

A Mathematical Framework for Deep Learning in Elastic Source Imaging

Jaejun Yoo^{a,b}, Abdul Wahab^{a,c}, Jong Chul Ye^{a,d,*}

^a*Bio-imaging and Signal Processing Laboratory, Department of Bio and Brain Engineering, Korea Advanced Institute of Science and Technology, 291 Daehak-ro, Yuseong-gu, 34141, Daejeon, South Korea*

^b*Clova AI Research, NAVER Corporation, Naver Green Factory, 6 Buljeong-ro, Bundang-gu, Seongnam-si, Gyeonggi-do, 13561, Korea*

^c*Department of Mathematics, University of Education, Attock Campus 43600, Pakistan*

^d*Department of Mathematical Sciences, Korea Advanced Institute of Science and Technology, 291 Daehak-ro, Yuseong-gu, 34141, Daejeon, South Korea*

Abstract

An inverse elastic source problem with sparse measurements is of concern. A generic mathematical framework is proposed which incorporates a low-dimensional manifold regularization in the conventional source reconstruction algorithms thereby enhancing their performance with sparse datasets. It is rigorously established that the proposed framework is equivalent to the so-called *deep convolutional framelet expansion* in machine learning literature for inverse problems. Apposite numerical examples are furnished to substantiate the efficacy of the proposed framework.

Keywords: elasticity imaging, inverse source problem, deep learning, time-reversal

2000 MSC: 35R30, 74D99, 92C55

1. Introduction

An abundance of real-world inverse problems, for instance in biomedical imaging, non-destructive testing, geological exploration, and sensing of seismic events, is concerned with the spatial and/or temporal support localization of *sources* generating wave fields in acoustic, electromagnetic, or elastic media (see, e.g., [1–9] and references therein). Numerous application-specific algorithms have been proposed in the recent past to procure solutions of diverse *inverse source problems* from time-series or time-harmonic measurements of thereby generated waves (see, e.g., [10–19]). The *inverse elastic source problems* are of

*Corresponding author

Email addresses: jaejun.yoo@navercorp.com (Jaejun Yoo), wahab@kaist.ac.kr (Abdul Wahab), jong.ye@kaist.ac.kr (Jong Chul Ye)

particular interest in this paper due to their relevance in so-called *elastography* [6–8, 20]. Another potential application is the localization of the background noise source distribution of earth, which contains significant information about the regional geology, time-dependent crustal changes and earthquakes [4, 5, 21, 22].

Most of the conventional algorithms are suited to continuous measurements, in other words, to experimental setups allowing to measure wave fields at each point inside a region of interest or on a substantial part of its boundary. In practice, this requires mechanical systems that furnish discrete data sampled on a very fine grid conforming to the Nyquist sampling rate. Unfortunately, this is not practically feasible due to mechanical, computational, and financial constraints. In this article, we are therefore interested in the problem of elastic source imaging with very sparse data, both in space and time, for which the image resolution furnished by the conventional algorithms degenerates. In order to explain the idea of the proposed framework, we will restrict ourselves to the *time-reversal technique* for elastic source localization presented by Ammari et al. [44] as the base conventional algorithm due to its robustness and efficiency. We precise that any other contemporary algorithm can be adopted accordingly. The interested readers are referred to the articles [3, 10, 16, 21, 44, 45] and reference cited therein for further details on time-reversal techniques for inverse source problems and their mathematical analysis.

One potential remedy to overcome the limitation of the conventional algorithms is to incorporate the smoothness penalty such as the total variation (TV) or other sparsity-inducing penalties under a data fidelity term. These approaches are, however, computationally expensive due to the repeated applications of forward solver and the reconstruction step during iterative updates. Direct image domain processing using these penalty could bypass the iterative applications of forward and inverse steps, but the performance improvements are not remarkable.

Recently, deep learning approaches have achieved tremendous success in various inverse problem [23–36]. In photo-acoustic tomography, Antholzer et al. [37] proposed a U-Net architecture [38] to effectively remove streaking artifacts from inverse spherical radon transform based reconstructed images. In spite of such intriguing performance improvement by deep learning approaches, the origin of the success for inverse problems was poorly understood. To address this, we recently proposed so-called *deep convolutional framelets* as a powerful mathematical framework to understand deep learning approaches for inverse problems [39]. The novelty of the deep convolutional framelets was the discovery that encoder-decoder network structure emerges from the Hankel matrix decomposition [39]. In addition, by controlling the number of filter channels, a neural network is trained to learn the optimal local bases so that it gives the best low-rank shrinkage [39]. This discovery demonstrates an important link between the deep learning and the compressed sensing approach [40] through a Hankel structure matrix decomposition [41–43].

Thus, the aim of this paper is to provide a deep learning reconstruction formula for elastic source imaging from sparse measurements. Specifically, we

provide a generic framework that incorporates a low-dimensional manifold regularization in the conventional reconstruction frameworks in order to achieve an image resolution comparable to that furnished by the continuous/dense measurements. As it will be explained later on, the resulting algorithm is equivalent to the deep convolutional framelet expansion for inverse problems [39].

The rest of this paper is organized as follows. The inverse elastic source problem dealt with in this article is introduced in Section 2 both in discrete and continuous settings. A brief review of the time-reversal algorithm is also provided in Section 2. The mathematical foundations of the deep learning approach for elastic source imaging are furnished in Section 3. Section 4 is dedicated to the design and training of the deep neural network. A few numerical examples are furnished in Section 5. The article ends with a brief summary of the key results in Section 6.

2. Problem Formulation

In this section, we first mathematically formulate the inverse elastic source problems with continuous and discrete measurements. Then, we briefly review the time-reversal technique for source imaging (with continuous data) as discussed in [44] in order to make the paper self-contained.

2.1. Inverse Elastic Source Problem with Continuous Measurements

Let $\mathbf{S} : \mathbb{R}^d \times \mathbb{R} \rightarrow \mathbb{R}^d$ be a compactly supported function. Then, the wave propagation in a linear isotropic elastic medium loaded in \mathbb{R}^d ($d = 2, 3$) is governed by the Lamé system,

$$\begin{cases} \frac{\partial^2 \mathbf{u}}{\partial t^2}(\mathbf{x}, t) - \mathcal{L}_{\lambda, \mu} \mathbf{u}(\mathbf{x}, t) = \mathbf{S}(\mathbf{x}, t), & (\mathbf{x}, t) \in \mathbb{R}^d \times \mathbb{R}, \\ \mathbf{u}(\mathbf{x}, t) = \mathbf{0} = \frac{\partial \mathbf{u}}{\partial t}(\mathbf{x}, t), & \mathbf{x} \in \mathbb{R}^d, t < 0, \end{cases} \quad (1)$$

where $\mathbf{u} = (u_1, \dots, u_d)^\top : \mathbb{R}^d \times \mathbb{R} \rightarrow \mathbb{R}^d$ is the elastic wave field generated by the source \mathbf{S} and $\mathcal{L}_{\lambda, \mu}$ is the linear isotropic elasticity operator,

$$\mathcal{L}_{\lambda, \mu} \mathbf{u} = \mu \Delta \mathbf{u} + (\lambda + \mu) \nabla (\nabla \cdot \mathbf{u}), \quad (2)$$

with Lamé parameters of the medium (λ, μ) and superscript \top indicating the transpose operation. Here, it is assumed for simplicity that the volume density of the medium is unit, i.e., λ , μ , and \mathbf{S} are density normalized. Moreover, the source is punctual in time, i.e., $\mathbf{S}(\mathbf{x}, t) = \mathbf{F}(\mathbf{x}) d\delta_0(t)/dt$, where δ_0 denotes the Dirac mass at 0 and its derivative is defined in the sense of distributions.

In this article, our quantity of interest is the spatial distribution of the source $\mathbf{F}(\mathbf{x}) = (F_1, \dots, F_d)^\top \in \mathbb{R}^d$. We precise that the source \mathbf{F} and the wave field \mathbf{u} are vectors in \mathbb{R}^d and can be decomposed in terms of irrotational components (or pressure components polarizing along the direction of propagation) and solenoidal components (or shear components polarizing along the direction

orthogonal to the direction of propagation). In particular, in a two-dimensional frame-of-reference wherein x - and y -axes are aligned with and orthogonal to the direction of propagation, respectively, the x - and y -components of the source \mathbf{F} are its pressure and shear components, respectively (see, e.g., Fig. 1 for the imaging setup).

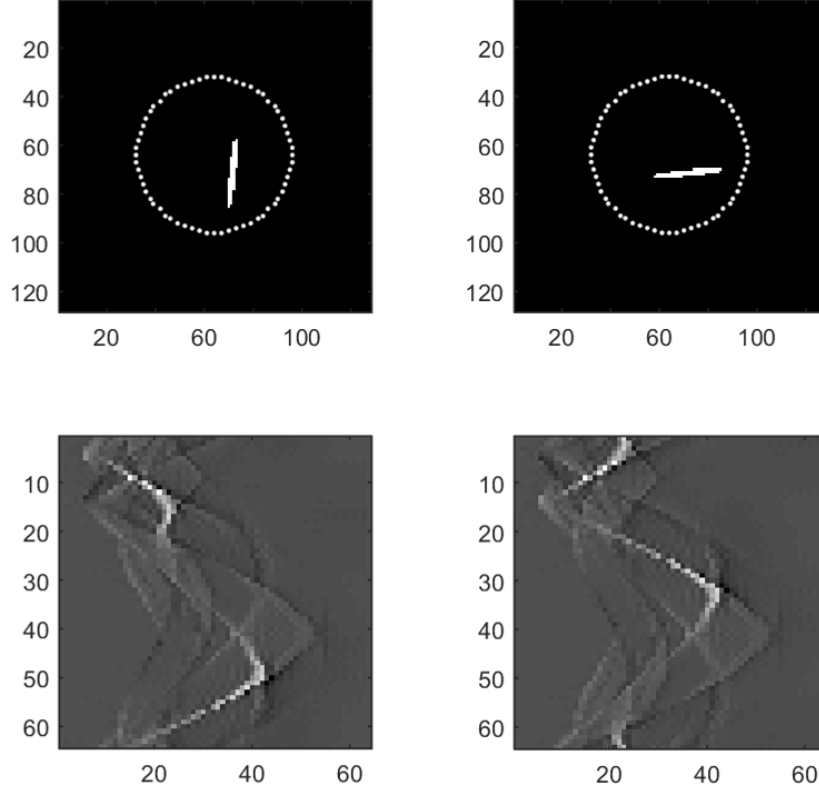


Figure 1: Source and measurement configuration in two-dimensions when the wave propagation direction is along the x -axis, the region of interest Ω is the unit disc centered at origin, 64 detectors are placed at the control geometry $\partial\Omega$ with a time interval $[0, 2s]$, the temporal scanning rate is $2^{-6}s$ and the displayed region is $[-2, 2]^2$ discretized with a mesh size 2^{-7} . Top: The pressure component (or x -component) (left) and the shear component (or y -component) (right) of the spatial support of the source density \mathbf{F} . Bottom: Measurements of the x -component (left) and y -component (right) of the wave field \mathbf{u} at $\partial\Omega$ (scanning times versus detector positions).

Let $\Omega \subset \mathbb{R}^d$ be an open bounded smooth imaging domain with \mathcal{C}^2 -boundary $\partial\Omega$, compactly containing the spatial support of \mathbf{F} , denoted by $\text{supp}\{\mathbf{F}\}$, i.e., there exists a compact set $\Omega^* \subset \mathbb{R}^d$ strictly contained in Ω such that $\text{supp}\{\mathbf{F}\} \subset \Omega^* \subset \Omega$. Then, the inverse elastic source problem with continuous measurement

data is to recover $\text{supp}\{\mathbf{F}\}$ given the measurements

$$\left\{ \mathbf{d}(\mathbf{y}, t) := \mathbf{u}(\mathbf{y}, t) \mid \forall \mathbf{y} \in \partial\Omega, \quad \forall t \in (0, t_{\max}) \right\}, \quad (3)$$

where t_{\max} is the final control time such that $\mathbf{u}(\mathbf{x}, t_{\max}) \approx 0$ and $\partial_t \mathbf{u}(\mathbf{x}, t_{\max}) \approx 0$ for all $\mathbf{x} \in \partial\Omega$.

2.2. Inverse Elastic Source Problem with Discrete Measurements

Most of the conventional algorithms require the measurement domain $\partial\Omega \times (0, t_{\max})$ to be sampled at the Nyquist sampling rate so that a numerical reconstruction of the spatial support is achieved at a high resolution. Specifically, the distance between consecutive receivers is taken to be less than half of the wavelength corresponding to the smallest frequency in the bandwidth and the temporal scanning is done at a fine rate so that the relative difference between consecutive scanning times is very small.

In practice, it is not feasible to place a large number of receivers at the boundary of the imaging domain and most often the measurements are available only at a few detectors (relative to the number of those required at the Nyquist sampling rate). As a result, one can not expect well-resolved reconstructed images from the conventional algorithms requiring continuous or dense measurements.

In the rest of this subsection, we provide a mathematical formulation of the inverse elastic source problem for reconstructing the spatial support of the source \mathbf{F} from a discrete measurement dataset. Towards this end, we fix some notation upfront. For any sufficiently smooth function $v : \mathbb{R} \rightarrow \mathbb{R}$, we define its temporal Fourier transform by

$$\hat{v}(\omega) = \mathcal{F}_t[v](\omega) := \int_{\mathbb{R}} e^{i\omega t} v(t) dt, \quad (4)$$

where $\omega \in \mathbb{R}$ is the temporal frequency. Similarly, we define the spatial Fourier transform of an arbitrary smooth function $w : \mathbb{R}^d \rightarrow \mathbb{R}$ by

$$\hat{w}(\mathbf{k}) = \mathcal{F}_{\mathbf{x}}[w](\mathbf{k}) := \int_{\mathbb{R}^d} e^{-i\mathbf{k} \cdot \mathbf{x}} w(\mathbf{x}) d\mathbf{x}, \quad (5)$$

with spatial frequency $\mathbf{k} \in \mathbb{R}^d$. Let the function $\hat{\mathbf{G}}_{\omega}$ be the Kupradze matrix of fundamental solutions associated to the time-harmonic elastic wave equation, i.e.,

$$\mathcal{L}_{\lambda, \mu}[\hat{\mathbf{G}}_{\omega}](\mathbf{x}) + \omega^2 \hat{\mathbf{G}}_{\omega}(\mathbf{x}) = -\delta_{\mathbf{0}}(\mathbf{x}) \mathbf{I}_d, \quad \mathbf{x} \in \mathbb{R}^d, \quad (6)$$

where $\mathbf{I}_d \in \mathbb{R}^{d \times d}$ is the identity matrix. For later use, we decompose $\hat{\mathbf{G}}$ into its shear and pressure parts as

$$\hat{\mathbf{G}}_{\omega}(\mathbf{x}) = \hat{\mathbf{G}}_{\omega}^P(\mathbf{x}) + \hat{\mathbf{G}}_{\omega}^S(\mathbf{x}), \quad \mathbf{x} \neq \mathbf{0}, \quad (7)$$

such that

$$\hat{\mathbf{G}}_{\omega}^P(\mathbf{x}) = -\frac{1}{\omega^2} \nabla \nabla^{\top} \hat{g}_{\omega}^P(\mathbf{x}) \quad \text{and} \quad \hat{\mathbf{G}}_{\omega}^S(\mathbf{x}) = \frac{1}{\omega^2} (\kappa_S^2 \mathbf{I}_d + \nabla \nabla^{\top}) \hat{g}_{\omega}^S(\mathbf{x}), \quad (8)$$

where

$$\widehat{g}_\omega^\alpha(\mathbf{x}) = \begin{cases} \frac{\iota}{4} H_0^{(1)}(\kappa_\alpha |\mathbf{x}|), & d = 2, \\ \frac{1}{4\pi |\mathbf{x}|} e^{i\kappa_\alpha |\mathbf{x}|}, & d = 3, \end{cases} \quad \text{and} \quad \kappa_\alpha := \frac{\omega}{c_\alpha} \quad \text{with} \quad \alpha = P, S. \quad (9)$$

Here, $H_0^{(1)}$ denotes the first-kind Hankel function of order 0, and $c_P = \sqrt{\lambda + 2\mu}$ and $c_S = \sqrt{\mu}$ are the pressure and shear wave speeds, respectively.

If $\mathbf{G}(\mathbf{x}, t) := \mathcal{F}_t^{-1}[\widehat{\mathbf{G}}_\omega(\mathbf{x})]$ then, by invoking the Green's theorem,

$$\mathbf{d}(\mathbf{y}, t) = \mathbf{u}(\mathbf{y}, t)|_{\mathbf{y} \in \partial\Omega} = \left[\int_{\Omega} \frac{\partial}{\partial t} \mathbf{G}(\mathbf{y} - \mathbf{z}, t) \mathbf{F}(\mathbf{z}) d\mathbf{z} \right] \bigg|_{\mathbf{y} \in \partial\Omega} =: \mathcal{D}[\mathbf{F}](\mathbf{y}, t), \quad (10)$$

for all $(\mathbf{y}, t) \in \partial\Omega \times [0, t_{\max}]$. Here, $\mathcal{D} : L^2(\Omega)^d \rightarrow L^2(\partial\Omega \times [0, T])^d$ denotes the source-to-measurement operator.

Let $\mathbf{y}_1, \dots, \mathbf{y}_M \in \partial\Omega$ be the locations of $M \in \mathbb{N}$ point receivers measuring the time-series of the outgoing elastic wave \mathbf{u} at instances $0 < t_1 < \dots < t_N < t_{\max}$ for some $N \in \mathbb{N}$. Then, the inverse elastic source problem with discrete data is to recover $\text{supp}\{\mathbf{F}\}$ given the discrete measurement set

$$\left\{ \mathbf{d}(\mathbf{y}_m, t_n) := \mathcal{D}[\mathbf{F}](\mathbf{y}_m, t_n) \mid \forall 1 \leq m \leq M, \quad 1 \leq n \leq N \right\}. \quad (11)$$

In this article, we are interested in the discrete inverse source problem with sparse data, i.e., when M and N are small relative to the Nyquist sampling rate.

In order to facilitate the ensuing discussion, let us introduce the discrete measurement vector $\mathcal{G} \in \mathbb{R}^{dMN}$ by

$$\mathcal{G} := \begin{pmatrix} \mathcal{G}_1 \\ \vdots \\ \mathcal{G}_d \end{pmatrix}, \quad \text{where} \quad \mathcal{G}_i := \begin{pmatrix} \mathcal{G}_i^1 \\ \vdots \\ \mathcal{G}_i^N \end{pmatrix} \quad \text{with} \quad \mathcal{G}_i^n := \begin{pmatrix} [\mathbf{d}(\mathbf{y}_1, t_n)]_i \\ \vdots \\ [\mathbf{d}(\mathbf{y}_M, t_n)]_i \end{pmatrix}. \quad (12)$$

Here and throughout this investigation, notation $[\cdot]_i$ indicates the i -th component of a vector and $[\cdot]_{ij}$ indicates the ij -th component of a matrix.

Let us also introduce the forward operator, $\mathcal{D}_{\text{dis}} : L^2(\mathbb{R}^d)^d \rightarrow \mathbb{R}^{dMN}$, in the discrete measurement case by

$$\mathcal{D}_{\text{dis}}[\mathbf{F}] := \begin{pmatrix} \mathcal{D}_1[\mathbf{F}] \\ \vdots \\ \mathcal{D}_d[\mathbf{F}] \end{pmatrix}, \quad \text{with} \quad \mathcal{D}_i[\mathbf{F}] := \begin{pmatrix} \mathcal{D}_i^1[\mathbf{F}] \\ \vdots \\ \mathcal{D}_i^N[\mathbf{F}] \end{pmatrix}, \quad (13)$$

where

$$\mathcal{D}_i^n[\mathbf{F}] := \begin{pmatrix} [\mathcal{D}[\mathbf{F}](\mathbf{y}_1, t_n)]_i \\ \vdots \\ [\mathcal{D}[\mathbf{F}](\mathbf{y}_M, t_n)]_i \end{pmatrix}. \quad (14)$$

Then, the inverse elastic source problem with discrete data is to recover \mathbf{F} from the relationship

$$\mathcal{G} = \mathcal{D}_{\text{dis}}[\mathbf{F}]. \quad (15)$$

2.3. Time-Reversal for Elastic Source Imaging: A Review

The idea of the time-reversal algorithm is based on a very simple observation that the wave operator in loss-less (non-attenuating) media is self-adjoint and that the corresponding Green's function possesses the reciprocity property [10]. In other words, the wave operator is invariant under time transformation $t \rightarrow -t$ and the positions of the sources and receivers can be swapped. Therefore, it is possible to theoretically *revert* a wave from the recording positions and different control times to the source locations and the initial time in chronology thereby converging to the source density. Practically, this is done by *back-propagating* the measured data, after transformation $t \rightarrow t_{\text{max}} - t$, through the adjoint waves \mathbf{v}_τ for each time instance $t = \tau$ and adding the contributions \mathbf{v}_τ for all $\tau \in (0, t_{\text{max}})$ after evaluating them at the final time $t = t_{\text{max}}$. Precisely, the adjoint wave \mathbf{v}_τ , for each $\tau \in (0, t_{\text{max}})$, is constructed as the solution to

$$\begin{cases} \frac{\partial^2 \mathbf{v}_\tau}{\partial t^2}(\mathbf{x}, t) - \mathcal{L}_{\lambda, \mu} \mathbf{v}_\tau(\mathbf{x}, t) = \frac{d\delta_\tau(t)}{dt} \mathbf{d}(\mathbf{x}, t_{\text{max}} - \tau) \delta_{\partial\Omega}(\mathbf{x}), & (\mathbf{x}, t) \in \mathbb{R}^d \times \mathbb{R}, \\ \mathbf{v}_\tau(\mathbf{x}, t) = \frac{\partial \mathbf{v}_\tau}{\partial t}(\mathbf{x}, t) = \mathbf{0}, & \mathbf{x} \in \mathbb{R}^d, t < \tau, \end{cases} \quad (16)$$

where $\delta_{\partial\Omega}$ is the surface Dirac mass on $\partial\Omega$. Then, the time-reversal imaging function is defined by

$$\mathcal{I}_{\text{TR}}(\mathbf{x}) = \int_0^{t_{\text{max}}} \mathbf{v}_\tau(\mathbf{x}, t_{\text{max}}) d\tau, \quad \mathbf{x} \in \Omega. \quad (17)$$

By the definition of the adjoint field \mathbf{v}_τ and the Green's theorem,

$$\mathbf{v}_\tau(\mathbf{x}, t) = \int_{\partial\Omega} \frac{\partial}{\partial t} \mathbf{G}(\mathbf{x} - \mathbf{y}, t - \tau) \mathbf{d}(\mathbf{y}, t_{\text{max}} - \tau) d\sigma(\mathbf{y}). \quad (18)$$

Therefore, the time-reversal function can be explicitly expressed as

$$\begin{aligned} \mathcal{I}_{\text{TR}}(\mathbf{x}) &= \int_0^{t_{\text{max}}} \int_{\partial\Omega} \int_{\Omega} \left[\frac{\partial}{\partial t} \mathbf{G}(\mathbf{x} - \mathbf{y}, t - \tau) \right] \bigg|_{t=t_{\text{max}}} \\ &\quad \times \left[\frac{\partial}{\partial t} \mathbf{G}(\mathbf{y} - \mathbf{z}, t) \mathbf{F}(\mathbf{z}) \right] \bigg|_{t=t_{\text{max}} - \tau} d\mathbf{z} d\sigma(\mathbf{y}) d\tau. \end{aligned} \quad (19)$$

The time-reversal function \mathcal{I}_{TR} in (17) is usually adopted to reconstruct the source distribution in an elastic medium. However, it does not provide a good reconstruction due to a non-linear coupling between the shear and pressure parts of the elastic field \mathbf{u} at the boundary, especially when the sources are

extended [3, 21, 44]. In fact, these components propagate at different wave-speeds and polarization directions, and cannot be separated at the surface of the imaging domain. If we simply back-propagate the measured data then the time-reversal operation mixes the components of the recovered support of the density \mathbf{F} . Specifically, it has been established in [44] that, by time reversing and back-propagating the elastic wave field signals as in (17), only a blurry image can be reconstructed together with an additive term introducing the coupling artifacts.

As a simple remedy for the coupling artifacts, a surgical procedure is proposed in [44] taking the leverage of a *Helmholtz decomposition* of \mathcal{I}_{TR} , (regarded as an *initial guess*). A weighted time-reversal imaging function (denoted by \mathcal{I}_{WTR} hereinafter) is constructed by separating the shear and pressure components of \mathcal{I}_{TR} as

$$\mathcal{I}_{\text{TR}} = \nabla \times \psi_{\mathcal{I}_{\text{TR}}} + \nabla \phi_{\mathcal{I}_{\text{TR}}}, \quad (20)$$

and then taking their weighted sum wherein the weights are respective wave speeds and the functions $\psi_{\mathcal{I}_{\text{TR}}}$ and $\phi_{\mathcal{I}_{\text{TR}}}$ are obtained by solving a weak Neumann problem. Precisely, \mathcal{I}_{WTR} is defined by

$$\mathcal{I}_{\text{WTR}} = c_S \nabla \times \psi_{\mathcal{I}_{\text{TR}}} + c_P \nabla \phi_{\mathcal{I}_{\text{TR}}}. \quad (21)$$

In fact, thanks to the Parseval's theorem and the fact that \mathbf{F} is compactly supported inside $\Omega \subset \mathbb{R}^d$, it can be established that

$$\begin{aligned} \mathcal{I}_{\text{WTR}}(\mathbf{x}) = \frac{1}{4\pi} \int_{\mathbb{R}^d} \int_{\mathbb{R}} \omega^2 \left[\int_{\partial\Omega} \left(\widehat{\mathbf{\Gamma}}_{\omega}(\mathbf{x} - \mathbf{y}) \overline{\widehat{\mathbf{G}}_{\omega}(\mathbf{y} - \mathbf{z})} \right. \right. \\ \left. \left. + \overline{\widehat{\mathbf{\Gamma}}_{\omega}(\mathbf{x} - \mathbf{y})} \widehat{\mathbf{G}}_{\omega}(\mathbf{y} - \mathbf{z}) \right) d\sigma(\mathbf{y}) \right] d\omega \mathbf{F}(\mathbf{z}) d\mathbf{z}, \end{aligned} \quad (22)$$

for a large final control time t_{max} with

$$\widehat{\mathbf{\Gamma}}_{\omega}(\mathbf{x}) := c_P \widehat{\mathbf{G}}_{\omega}^P(\mathbf{x}) + c_S \widehat{\mathbf{G}}_{\omega}^S(\mathbf{x}), \quad \forall \mathbf{x} \in \mathbb{R}^d.$$

After tedious manipulations, using the *elastic Helmholtz-Kirchhoff identities* (see, e.g., [44, Proposition 2.5]), and assuming Ω to be a ball with radius $R \rightarrow +\infty$, one finds out that

$$\mathcal{I}_{\text{WTR}}(\mathbf{x}) \stackrel{R \rightarrow +\infty}{=} \frac{1}{2\pi} \int_{\mathbb{R}^d} \int_{\mathbb{R}} \omega \Im \left[\widehat{\mathbf{G}}_{\omega}(\mathbf{x} - \mathbf{z}) \right] d\omega \mathbf{F}(\mathbf{z}) d\mathbf{z}. \quad (23)$$

Since

$$\frac{1}{2\pi} \int_{\mathbb{R}} -i\omega \widehat{\mathbf{G}}_{\omega}(\mathbf{x} - \mathbf{z}) d\omega = \delta_{\mathbf{x}}(\mathbf{z}) \mathbf{I}_d, \quad (24)$$

which comes from the integration of the time-dependent version of Eq. (6) between $t = 0^-$ and $t = 0^+$, the following result holds (see, e.g., [44, Theorem 2.6]).

Theorem 2.1. *Let Ω be a ball in \mathbb{R}^d with large radius R . Let $\mathbf{x} \in \Omega$ be sufficiently far from the boundary $\partial\Omega$ with respect to the wavelength and \mathcal{I}_{WTR} be defined by (21). Then,*

$$\mathcal{I}_{\text{WTR}}(\mathbf{x}) \underset{R \rightarrow +\infty}{=} \mathbf{F}(\mathbf{x}). \quad (25)$$

We conclude this section with the following remarks. Let \mathcal{D} be the source-to-measurement operator, defined in (10). Then, it is easy to infer from Theorem 2.1 that its inverse (or the measurement-to-source) operator is given by

$$\mathcal{D}^{-1}[\mathbf{d}](\mathbf{x}) \underset{R \rightarrow +\infty}{=} \mathcal{I}_{\text{WTR}}(\mathbf{x}), \quad (26)$$

when imaging domain Ω is a ball with large radius R . However, there are a few technical limitations. Firstly, if the imaging domain Ω is not *sufficiently large* as compared to the characteristic size of the support of \mathbf{F} , which in turn should be sufficiently localized at the *center* of the imaging domain (i.e., located far away from the boundary $\partial\Omega$), one can only get an approximation of \mathbf{F} which may not be very well-resolved. Moreover, \mathcal{I}_{WTR} may not be able to effectively rectify the coupling artifacts in that case, as it has been substantiated for extended sources in [44]. Secondly, like most of the contemporary conventional techniques, time-reversal algorithm requires continuous measurements (or dense measurements at the Nyquist sampling rate). Therefore, as will be highlighted later on in the subsequent sections, very strong streaking artifacts appear when the time-reversal algorithm is applied with sparse measurements. In order to overcome these issues, we discuss a deep learning approach in the next section.

3. Deep Learning Approach for Inverse Elastic Source Problem

Let us consider the inverse elastic source problem with sparse measurements. Our aim is to recover \mathbf{F} from the relationship (15). Unfortunately, due to sub-sampling, Eq. (15) is not uniquely solvable. In fact, the null space, $\mathcal{N}(\mathcal{D}_{\text{dis}})$, of the forward operator \mathcal{D}_{dis} is non-empty, i.e., there exist non-zero functions, $\mathbf{F}^0 \in L^2(\mathbb{R}^d)^d$, such that

$$\mathcal{D}_{\text{dis}}(\mathbf{F}^0) = \mathbf{0}. \quad (27)$$

In particular, the existence of the non-radiating parts of the source makes the solution non-unique. This suggests that there are infinite many feasible solutions to the discrete problem (15). Hence, the application of the time-reversal algorithm requiring the availability of continuous or dense measurements results in strong imaging artifacts severely affecting the resolution of the reconstruction.

A typical way to avoid the non-uniqueness of the solution from sparse measurements is the use of regularization. Accordingly, many regularization techniques have been proposed over the past few decades. Among various penalties for regularized reconstruction, here our discussion begins with a structured low-rank penalty [41], which is closely related to the deep learning approach adopted in this investigation.

3.1. Generic Inversion Formula under Structured Low-Rank Constraint

Let $\{\mathbf{z}_q\}_{q=1}^Q \subset \Omega$, for some integer $Q \in \mathbb{N}$, be a collection of finite number of sampling points of the region of interest Ω confirming to the Nyquist sampling rate. In this section, we look for a (discrete) approximation of the density \mathbf{F} and choose a piece-wise constant or spline ansatz as

$$[\mathbf{F}(\mathbf{z})]_i := \sum_{q=1}^Q [\mathbf{F}(\mathbf{z}_q)]_i \vartheta_i(\mathbf{z}, \mathbf{z}_q), \quad \forall \mathbf{z} \in \Omega, \quad (28)$$

where $\vartheta_i(\cdot, \mathbf{z}_q)$ is the basis function for the i -th coordinate, associated with the sampling point \mathbf{z}_q . We introduce the discretized source density to be sought by

$$\mathbf{f} := \begin{pmatrix} \mathbf{f}_1 \\ \vdots \\ \mathbf{f}_d \end{pmatrix} \in \mathbb{R}^{dQ} \quad \text{with} \quad \mathbf{f}_i := \begin{pmatrix} [\mathbf{F}(\mathbf{z}_1)]_i \\ \vdots \\ [\mathbf{F}(\mathbf{z}_Q)]_i \end{pmatrix}. \quad (29)$$

Let us define the row-vector $\mathbf{\Lambda}_{i,j}^{n,m} \in \mathbb{R}^{1 \times Q}$ by

$$[\mathbf{\Lambda}_{i,j}^{n,m}]_q := \int_{\Omega} \left[\frac{\partial}{\partial t} \mathbf{G}(\mathbf{y}_m - \mathbf{z}, t) \right]_{ij} \bigg|_{t=t_n} \vartheta_j(\mathbf{z}, \mathbf{z}_q) d\mathbf{z}. \quad (30)$$

Accordingly, we define the sensing matrix $\mathbf{\Lambda} \in \mathbb{R}^{dNM \times dQ}$ by

$$\mathbf{\Lambda} := \begin{pmatrix} \mathbf{\Lambda}_1 \\ \vdots \\ \mathbf{\Lambda}_d \end{pmatrix}, \quad \text{where} \quad \mathbf{\Lambda}_i := \begin{pmatrix} \mathbf{\Lambda}_i^1 \\ \vdots \\ \mathbf{\Lambda}_i^N \end{pmatrix} \quad \text{with} \quad \mathbf{\Lambda}_i^n := \begin{pmatrix} \mathbf{\Lambda}_{i1}^{n,1} & \cdots & \mathbf{\Lambda}_{id}^{n,1} \\ \mathbf{\Lambda}_{i1}^{n,2} & \cdots & \mathbf{\Lambda}_{id}^{n,2} \\ \vdots & \ddots & \vdots \\ \mathbf{\Lambda}_{i1}^{n,M} & \cdots & \mathbf{\Lambda}_{id}^{n,M} \end{pmatrix}. \quad (31)$$

Then, the discrete version of the relationship (15) between measurements and the source is given by

$$\mathcal{G} \approx \mathbf{\Lambda} \mathbf{f}. \quad (32)$$

In order to facilitate the ensuing discussion, we define the wrap-around structured Hankel matrix associated to an arbitrary vector $\mathbf{f}_i \in \mathbb{R}^Q$, for $i = 1, \dots, d$, by

$$\mathbb{H}_{p_i}(\mathbf{f}_i) := \begin{pmatrix} [\mathbf{f}_i]_1 & [\mathbf{f}_i]_2 & \cdots & [\mathbf{f}_i]_p \\ [\mathbf{f}_i]_2 & [\mathbf{f}_i]_3 & \cdots & [\mathbf{f}_i]_{p+1} \\ \vdots & \vdots & \ddots & \vdots \\ [\mathbf{f}_i]_Q & [\mathbf{f}_i]_1 & \cdots & [\mathbf{f}_i]_{p-1} \end{pmatrix}, \quad (33)$$

where $p_i < Q$ is the so-called matrix-pencil size. It is known (see, e.g., [41]) that if the coordinate function $[\mathbf{F}]_i$ corresponds to a smoothly varying perturbation or it has either edges or patterns then the corresponding Fourier spectrum

$\hat{f}(\mathbf{k})$ is mostly concentrated in a small number of coefficients. Thus, if \mathbf{f}_i is a discretization of $[\mathbf{F}]_i$ at the Nyquist sampling rate then the associated Hankel structured matrix $\mathbb{H}_{p_i}(\mathbf{f}_i) \in \mathbb{R}^{Q \times p_i}$ in the image domain is low-ranked. We refer the interested readers to [41] for further details. In the same way, we expect that the block Hankel structured matrix of the discrete source vector \mathbf{f} , constructed as

$$\mathbb{H}_p(\mathbf{f}) = \begin{pmatrix} \mathbb{H}_{p_1}(\mathbf{f}_1) & \cdots & \mathbf{0} \\ \vdots & \ddots & \vdots \\ \mathbf{0} & \cdots & \mathbb{H}_{p_d}(\mathbf{f}_d) \end{pmatrix} \in \mathbb{R}^{dQ \times p}, \quad (34)$$

is low-rank. Therefore, a generic form of the low-rank Hankel structured constrained inverse problem can be formulated as

$$\begin{aligned} \min_{\mathbf{f} \in \mathbb{R}^{dQ}} \quad & \|\mathcal{G} - \mathbf{A}\mathbf{f}\|^2 \\ \text{subject to} \quad & \text{RANK}(\mathbb{H}_p(\mathbf{f})) \leq r = \sum_{i=1}^d r_i < p = \sum_{i=1}^d p_i, \end{aligned} \quad (35)$$

where $\text{RANK}(\cdot)$ denotes the rank of a matrix and $r_i \in \mathbb{N}$.

It is clear that, for a feasible solution $\mathbf{f} = (\mathbf{f}_1^\top, \dots, \mathbf{f}_d^\top)^\top$ of the regularization problem (35), the Hankel structured matrix $\mathbb{H}_{p_i}(\mathbf{f}_i)$, for $i = 1, \dots, d$, admits the singular value decomposition $\mathbb{H}_{p_i}(\mathbf{f}_i) = \mathbf{U}^i \mathbf{\Sigma}^i (\mathbf{V}^i)^\top$, where $\mathbf{U}^i = (\mathbf{u}_1^i, \dots, \mathbf{u}_{r_i}^i) \in \mathbb{R}^{Q \times r_i}$ and $\mathbf{V}^i = (\mathbf{v}_1^i, \dots, \mathbf{v}_{r_i}^i) \in \mathbb{R}^{p_i \times r_i}$ denote the left and the right singular vector bases matrices, respectively, and $\mathbf{\Sigma}^i = (\Sigma_{kl}^i)_{k,l=1}^{r_i} \in \mathbb{R}^{r_i \times r_i}$ refers to the diagonal matrix with singular values as elements. If there exist two pairs of matrices $\mathbf{\Phi}_i, \tilde{\mathbf{\Phi}}_i \in \mathbb{R}^{Q \times S}$ and $\mathbf{\Psi}_i, \tilde{\mathbf{\Psi}}_i \in \mathbb{R}^{p_i \times r_i}$, for each $i = 1, \dots, d$ and $S \geq Q$, satisfying the conditions

$$\tilde{\mathbf{\Phi}}_i \mathbf{\Phi}_i^\top = \mathbf{I}_Q \quad \text{and} \quad \mathbf{\Psi}_i \tilde{\mathbf{\Psi}}_i^\top = \mathbf{P}_{\mathcal{R}(\mathbf{V}^i)}, \quad (36)$$

then

$$\mathbb{H}_{p_i}(\mathbf{f}_i) = \tilde{\mathbf{\Phi}}_i \mathbf{\Phi}_i^\top \mathbb{H}_{p_i}(\mathbf{f}_i) \mathbf{\Psi}_i \tilde{\mathbf{\Psi}}_i^\top = \tilde{\mathbf{\Phi}}_i \mathbf{C}_i(\mathbf{f}_i) \tilde{\mathbf{\Psi}}_i^\top, \quad (37)$$

with the transformation $\mathbf{C}_i : \mathbb{R}^Q \rightarrow \mathbb{R}^{S \times r_i}$ given by

$$\mathbf{C}_i(\mathbf{g}) = \mathbf{\Phi}_i^\top \mathbb{H}_{p_i}(\mathbf{g}) \mathbf{\Psi}_i, \quad \forall \mathbf{g} \in \mathbb{R}^Q. \quad (38)$$

Here, the first condition in (36) is the so-called *frame condition*, $\mathcal{R}(\mathbf{V}^i)$ denotes the range space of \mathbf{V}^i and $\mathbf{P}_{\mathcal{R}(\mathbf{V}^i)}$ represents a projection onto $\mathcal{R}(\mathbf{V}^i)$ [39]. Precisely, (37) is equivalent to the paired encoder-decoder convolution structure

$$\mathbf{C}_i(\mathbf{f}_i) = \mathbf{\Phi}_i^\top (\mathbf{f}_i \circledast \mathbf{\Psi}_i'), \quad (39)$$

$$\mathbf{f}_i = \left(\tilde{\mathbf{\Phi}}_i \mathbf{C}_i \right) \circledast \zeta_i \left(\tilde{\mathbf{\Psi}}_i \right), \quad (40)$$

where the convolutions in (39) and (40) correspond to the multi-channel convolutions with the associated filters,

$$\mathbf{\Psi}'_i := (\boldsymbol{\psi}'_{i1}, \dots, \boldsymbol{\psi}'_{ir_i}) \in \mathbb{R}^{p_i \times r_i}, \quad \zeta_i(\tilde{\mathbf{\Psi}}_i) := \frac{1}{p_i} \begin{pmatrix} \tilde{\boldsymbol{\psi}}_{i1} \\ \vdots \\ \tilde{\boldsymbol{\psi}}_{ir_i} \end{pmatrix} \in \mathbb{R}^{p_i r_i}. \quad (41)$$

Here, the superposed prime over $\boldsymbol{\psi}_{ik} \in \mathbb{R}^{p_i}$, for fixed $i = 1, \dots, d$, and $k = 1, \dots, r_i$, indicates its flipped version, i.e., the indices of $\boldsymbol{\psi}_{ik}$ are reversed [41].

Let us introduce the block matrices

$$\begin{aligned} \mathbf{\Phi} &= \text{DIAG}(\mathbf{\Phi}_1, \dots, \mathbf{\Phi}_d), & \tilde{\mathbf{\Phi}} &= \text{DIAG}(\tilde{\mathbf{\Phi}}_1, \dots, \tilde{\mathbf{\Phi}}_d), \\ \mathbf{\Psi} &= \text{DIAG}(\mathbf{\Psi}_1, \dots, \mathbf{\Psi}_d), & \tilde{\mathbf{\Psi}} &= \text{DIAG}(\tilde{\mathbf{\Psi}}_1, \dots, \tilde{\mathbf{\Psi}}_d), \\ \mathbf{V} &= \text{DIAG}(\mathbf{V}_1, \dots, \mathbf{V}_d). \end{aligned} \quad (42)$$

Then, thanks to conditions in (36), the pair of matrices $(\mathbf{\Phi}, \tilde{\mathbf{\Phi}})$ satisfy the frame condition

$$\tilde{\mathbf{\Phi}} \mathbf{\Phi}^\top = \mathbf{I}_{dQ} \quad \text{and} \quad \mathbf{\Psi} \tilde{\mathbf{\Psi}}^\top = \mathbf{P}_{\mathcal{R}(\mathbf{V})}, \quad (43)$$

Consequently, we have

$$\mathbb{H}_p(\mathbf{f}) = \tilde{\mathbf{\Phi}} \mathbf{\Phi}^\top \mathbb{H}_p(\mathbf{f}) \mathbf{\Psi} \tilde{\mathbf{\Psi}}^\top = \tilde{\mathbf{\Phi}} \mathbf{C}(\mathbf{f}) \tilde{\mathbf{\Psi}}^\top, \quad (44)$$

with the matrix transformation $\mathbf{C} : \mathbb{R}^{dQ} \rightarrow \mathbb{R}^{dS \times r}$ given by

$$\mathbf{C}(\mathbf{f}) = \text{DIAG}(\mathbf{C}_1(\mathbf{f}_1), \dots, \mathbf{C}_d(\mathbf{f}_d)) = \mathbf{\Phi}^\top \mathbb{H}_p(\mathbf{f}) \mathbf{\Psi}. \quad (45)$$

Let \mathcal{H}_i , for each $i = 1, \dots, d$, refer to the space of signals admissible in the form (39) and (40), i.e.,

$$\mathcal{H}_i := \left\{ \mathbf{g}_i \in \mathbb{R}^Q \mid \mathbf{g}_i = \left(\tilde{\mathbf{\Phi}}_i \mathbf{C}_i \right) \circledast \zeta_i \left(\tilde{\mathbf{\Psi}}_i \right), \mathbf{C}_i = \mathbf{\Phi}_i^\top (\mathbf{g}_i \circledast \mathbf{\Psi}'_i), \right\}. \quad (46)$$

Then, the problem (35) can be converted to

$$\min_{\mathbf{f} \in \prod_{i=1}^d \mathcal{H}_i} \|\mathcal{G} - \mathbf{\Lambda} \mathbf{f}\|^2, \quad (47)$$

or equivalently,

$$\min_{\mathbf{f}_i \in \mathcal{H}_i} \|\mathcal{G}_i - \mathbf{\Lambda}_i \mathbf{f}_i\|^2, \quad i = 1, \dots, d, \quad (48)$$

where the sub-matrices \mathcal{G}_i and $\mathbf{\Lambda}_i$ are defined in Eqs. (12) and (31), respectively.

3.2. Learning Based Regularization under Structured Low-Rank Constraint

In the previous section, the bases $(\Phi_i, \tilde{\Phi}_i)$ and $(\Psi_i, \tilde{\Psi}_i)$, for $i = 1, \dots, d$, are not specified in (36). The above discussion suggests that the pair of basis matrices $(\Phi_i, \tilde{\Phi}_i)$ is *non-local* in the sense that these matrices interact with all the components of the vector \mathbf{f}_i . On the other hand, the pair $(\Psi_i, \tilde{\Psi}_i)$ is *local* since these matrices interact with only p_i components of \mathbf{f}_i and can only be learned from the data itself. One of the most important discoveries in [39] is that an encoder-decoder network architecture in the convolutional neural network (CNN) is emerged from (37) and (38). In particular, the non-local bases matrices Φ_i and $\tilde{\Phi}_i$ play the role of *pooling* and *unpooling* operations, respectively (see, Section 3.3), whereas the local-bases Ψ_i and $\tilde{\Psi}_i$ corresponds to the *encoder and decoder layer convolutional filters* that have to be learned from the data [39].

Specifically, our goal is to learn $(\Psi_i, \tilde{\Psi}_i)$ in a *data-driven* fashion so that the optimization problem (47) (or equivalently (48)) can be simplified. Specifically, by defining Λ^\dagger (resp. Λ_i^\dagger) as a right pseudo-inverse of Λ (resp. Λ_i), i.e., $\Lambda\Lambda^\dagger\mathcal{G} = \mathcal{G}$ (resp. $\Lambda_i\Lambda_i^\dagger\mathcal{G}_i = \mathcal{G}_i$) for all $\mathcal{G} \in \mathbb{R}^{dMN}$, the cost in (47) (resp (48)) can be automatically minimized. However, the solution based on the right pseudo-inverse leads to

$$\Lambda^\dagger\mathcal{G} = \mathbf{f}^* + \mathbf{f}^0 := \begin{pmatrix} \mathbf{f}_1^* \\ \vdots \\ \mathbf{f}_d^* \end{pmatrix} + \begin{pmatrix} \mathbf{f}_1^0 \\ \vdots \\ \mathbf{f}_d^0 \end{pmatrix}, \quad (49)$$

where \mathbf{f}^* denotes the true solution and $\mathbf{f}^0 \in \mathcal{N}(\Lambda)$. Therefore, we look for the matrices $(\Psi_i, \tilde{\Psi}_i)$ such that

$$\mathbf{f}_i^* = \mathcal{K}_i(\mathbf{f}_i^* + \mathbf{f}_i^0) := \left(\tilde{\Phi}_i \mathbf{C}_i(\mathbf{f}_i^* + \mathbf{f}_i^0) \right) \otimes \zeta_i(\tilde{\Psi}_i), \quad \forall \mathbf{f}^0 \in \mathcal{N}(\Lambda), \quad i = 1, \dots, d, \quad (50)$$

where the operator $\mathcal{K}_i : \mathbb{R}^Q \rightarrow \mathcal{R}(\Lambda)$ is defined in terms of the mapping \mathbf{C}_i as

$$\mathcal{K}_i(\mathbf{g}) = \mathcal{K}_i(\mathbf{g}^r + \mathbf{g}^0) := \left(\tilde{\Phi}_i \mathbf{C}_i(\mathbf{g}^r + \mathbf{g}^0) \right) \otimes \zeta_i(\tilde{\Psi}_i), \quad \forall i = 1, \dots, d, \quad (51)$$

for all $\mathbf{g} = \mathbf{g}^r \oplus \mathbf{g}^0 \in \mathcal{R}(\Lambda) \oplus \mathcal{N}(\Lambda)$. In fact, the operator \mathcal{K}_i in (51) can be engineered so that its output belongs to $\mathcal{R}(\Lambda)$ by selecting the filter Ψ'_i that *annihilates* the null-space component \mathbf{g}^0 , i.e.,

$$\mathbf{g}^0 \otimes \Psi'_i \approx \mathbf{0}, \quad i = 1, \dots, d, \quad (52)$$

which implies that the block filter Ψ' should span the orthogonal complement of $\mathcal{N}(\Lambda)$. Therefore, the bases learning problem becomes

$$\min_{\mathcal{K}_i} \sum_{\ell=1}^L \left\| \mathbf{f}_i^{*(\ell)} - \mathcal{K}_i(\mathbf{f}_i^{(\ell)}) \right\|^2, \quad i = 1, \dots, d, \quad (53)$$

where

$$\left\{ \left(\mathbf{f}_i^{(\ell)}, \mathbf{f}_i^{*(\ell)} \right) := \left(\left[\mathbf{\Lambda}^\dagger \mathbf{G}^{(\ell)} \right]_i, \mathbf{f}_i^{*(\ell)} \right) \right\}_{\ell=1}^L,$$

denotes the training dataset composed of the input and ground-truth pairs.

The purpose of our neural network is to learn the local basis from the training data assuming that the Hankel matrices associated with discrete source densities \mathbf{f}_i are of rank r_i . In order to reduce the search space for the filters, we restrict the framelet coefficient matrices $\mathbf{C}_i(\mathbf{f}_i)$ to have positive elements only, i.e., we look for the unknowns in the signal subspace

$$\begin{aligned} \mathcal{H}_i^0 &:= \left\{ \mathbf{g} \in \mathbb{R}^Q \mid \mathbf{g} = \left(\tilde{\Phi}_i \mathbf{C}_i(\mathbf{g}) \right) \circledast \zeta_i \left(\tilde{\Psi}_i \right), \right. \\ &\quad \left. \mathbf{C}_i(\mathbf{g}) = \Phi_i^\top (\mathbf{g} \circledast \Psi_i'), \quad [\mathbf{C}_i(\mathbf{g})]_{kl} \geq 0, \forall k, l \right\}, \end{aligned} \quad (54)$$

for $i = 1, \dots, d$. In fact, the positivity constraint is justified since the input and label data for the neural network are normalized with appropriated bias [39]. Accordingly, the local basis learning problem (53) can equivalently be expressed as

$$\min_{(\Psi_i, \tilde{\Psi}_i)} \sum_{\ell=1}^L \left\| \mathbf{f}_i^{*(\ell)} - \mathcal{K}_i^\varrho \left(\mathbf{f}_i^{(\ell)}; \Psi_i, \tilde{\Psi}_i \right) \right\|^2, \quad i = 1, \dots, d. \quad (55)$$

Here, the operator $\mathcal{K}_i^\varrho : \mathbb{R}^Q \rightarrow \mathcal{R}(\mathbf{\Lambda})$ is defined analogously as in (51) but in terms of the mapping $\mathbf{C}_i^\varrho : \mathbb{R}^Q \rightarrow \mathbb{R}^{S \times r_i}$ given by

$$\mathbf{C}_i^\varrho(\mathbf{g}) = \varrho \left(\Phi_i^\top (\mathbf{g} \circledast \Psi_i') \right), \quad \forall i = 1, \dots, d, \quad (56)$$

with ϱ imposing the positivity constraint, i.e., for arbitrary matrix $\mathbf{A} \in \mathbb{R}^{S \times r_i}$, we have $[\varrho(\mathbf{A})]_{kl} \geq 0$, for all $k, l = 1, \dots, r_i$. In the context of deep learning this role is played by the *rectified linear unit* (ReLU) [46].

In general, for a multi-layer deep convolutional framelet expansion with $J \in \mathbb{N}$ layers, the signal space is recursively defined as

$$\begin{aligned} \mathcal{H}_i^0 &:= \left\{ \mathbf{g} \in \mathbb{R}^Q \mid \mathbf{g} = \left(\tilde{\Phi}_i \mathbf{C}_i(\mathbf{g}) \right) \circledast \zeta_i \left(\tilde{\Psi}_i \right), \right. \\ &\quad \left. \mathbf{C}_i(\mathbf{g}) = \Phi_i^\top (\mathbf{g} \circledast \Psi_i') \in \mathcal{H}_i^1, \quad [\mathbf{C}_i(\mathbf{g})]_{kl} \geq 0, \forall k, l \right\}, \end{aligned} \quad (57)$$

where, for all $j = 1, \dots, J-1 \in \mathbb{N}$,

$$\begin{aligned} \mathcal{H}_i^j &:= \left\{ \mathbf{A} \in \mathbb{R}^{Q \times Q_i^{(j)}} \mid \mathbf{A} = \left(\tilde{\Phi}_i \mathbf{C}_i^{(j)}(\mathbf{A}) \right) \circledast \zeta_i \left(\tilde{\Psi}_i^{(j)} \right), \right. \\ &\quad \left. \mathbf{C}_i^{(j)}(\mathbf{A}) = \Phi_i^\top \left(\mathbf{A} \circledast \Psi_i'^{(j)} \right) \in \mathcal{H}_i^{j+1}, \quad [\mathbf{C}_i(\mathbf{g})]_{kl} \geq 0, \forall k, l \right\}, \end{aligned} \quad (58)$$

$$\mathcal{H}_i^J := \mathbb{R}^{Q \times Q_i^{(J)}}. \quad (59)$$

Here, the j -th layer encoder and decoder filters are given by

$$\Psi_i^{(j)} := \begin{pmatrix} \psi_{i1}^{'1} & \cdots & \psi_{iR_i^{(j)}}^{'1} \\ \vdots & \ddots & \vdots \\ \psi_{i1}^{'Q_i^{(j)}} & \cdots & \psi_{iR_i^{(j)}}^{'Q_i^{(j)}} \end{pmatrix} \in \mathbb{R}^{p_i^{(j)} Q_i^{(j)} \times R_i^{(j)}}, \quad (60)$$

$$\zeta_i(\tilde{\Psi}_i^{(j)}) := \begin{pmatrix} \tilde{\psi}_{i1}^1 & \cdots & \tilde{\psi}_{i1}^{Q_i^{(j)}} \\ \vdots & \ddots & \vdots \\ \tilde{\psi}_{iR_i^{(j)}}^1 & \cdots & \tilde{\psi}_{iR_i^{(j)}}^{Q_i^{(j)}} \end{pmatrix} \in \mathbb{R}^{p_i^{(j)} R_i^{(j)} \times Q_i^{(j)}}, \quad (61)$$

where $p_i^{(j)}$, $Q_i^{(j)}$, and $R_i^{(j)}$ are the filter length, the number of input channels, and the number of output channels, respectively.

3.3. Dual-Frame U-Net

As discussed before, the non-local basis $\tilde{\Phi}_i, \Phi_i^\top$ corresponds to the generalized pooling and unpooling operations, which can be designed by the users for specific inverse problems. Here, the key requisite is the frame condition in (36), i.e., $\tilde{\Phi}_i \Phi_i^\top = \mathbf{I}_Q$. As the artifacts of the time-reversal recovery from sparse measurement is distributed globally, we need a network architecture with large receptive fields. Thus, in order to learn the optimal local basis from the minimization problem (53), we adopt the commonly used CNN architecture known as *U-Net* [38] and its deep convolutional framelets based variant, coined as *Dual-Frame U-Net* [47] (see Fig. 2). These networks have pooling layers with down sampling, resulting exponentially large receptive fields.

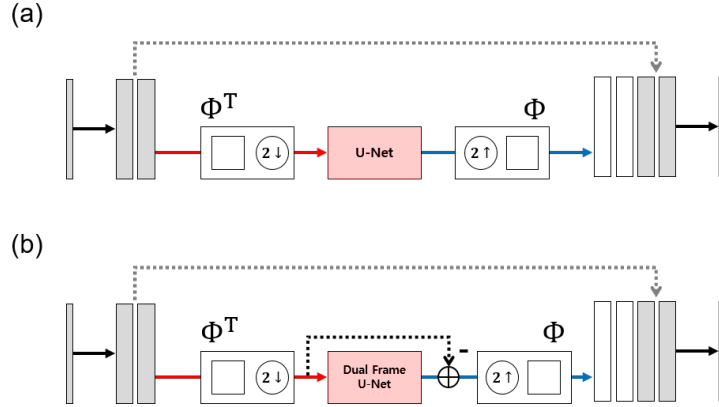


Figure 2: Simplified U-Net architecture and its variant. (a) Standard U-Net and (b) Dual-Frame U-Net.

However, as shown in [47], one of the main limitation of the standard U-Net is that it does not satisfy the frame condition in (36). Specifically, by considering

both skipped connection and the pooling Φ_i^\top in Fig. 2(a), the non-local basis for the standard U-Net is given by

$$\Phi_i^\top := \begin{pmatrix} \mathbf{I}_Q \\ \Phi_{i,\text{avg}}^\top \end{pmatrix} \in \mathbb{R}^{\frac{3Q}{2} \times Q}, \quad (62)$$

where $\Phi_{i,\text{avg}}^\top$ denotes an average pooling operator given by

$$\Phi_{i,\text{avg}}^\top = \frac{1}{\sqrt{2}} \begin{pmatrix} 1 & 1 & 0 & 0 & \cdots & 0 & 0 \\ 0 & 0 & 1 & 1 & \cdots & 0 & 0 \\ \vdots & \vdots & \vdots & \vdots & \ddots & \vdots & \vdots \\ 0 & 0 & 0 & 0 & \cdots & 1 & 1 \end{pmatrix} \in \mathbb{R}^{\frac{Q}{2} \times Q}. \quad (63)$$

Moreover, the unpooling layer in the standard U-Net is given by Φ_i . Therefore,

$$\tilde{\Phi}_i \Phi_i^\top = \mathbf{I}_Q + \Phi_{i,\text{avg}} \Phi_{i,\text{avg}}^\top \neq \mathbf{I}_Q. \quad (64)$$

Consequently, the frame condition in (36) is not satisfied. As shown in [39], this results in the duplication of the low-frequency components, making the final results blurry.

In order to address the aforementioned problem, in the Dual-Frame U-Net [47], the dual frame is directly implemented. More specifically, the dual frame $\tilde{\Phi}_i$ for the given frame operator (62) is given by

$$\begin{aligned} \tilde{\Phi}_i &:= (\Phi_i \Phi_i^\top)^{-1} \Phi_i = (\mathbf{I}_Q + \Phi_{i,\text{avg}} \Phi_{i,\text{avg}}^\top)^{-1} [\mathbf{I}_Q \quad \Phi_{i,\text{avg}}] \\ &= [\mathbf{I}_Q - \Phi_{i,\text{avg}} \Phi_{i,\text{avg}}^\top / 2 \quad \Phi_{i,\text{avg}} / 2], \end{aligned} \quad (65)$$

where we use the matrix inversion lemma and the orthogonality $\Phi_{i,\text{avg}}^\top \Phi_{i,\text{avg}} = \mathbf{I}_Q$ for the last equality. It was shown in [47] that the corresponding generalized unpooling operation is given by

$$\tilde{\Phi}_i \begin{bmatrix} \mathbf{B}_i \\ \mathbf{C}_i(\mathbf{g}) \end{bmatrix} = \mathbf{B}_i + \underbrace{\frac{1}{2} \Phi_{i,\text{avg}}}_{\text{unpooling}} \overbrace{(\mathbf{C}_i(\mathbf{g}) - \Phi_{i,\text{avg}}^\top \mathbf{B}_i)}^{\text{residual}}, \quad (66)$$

where \mathbf{B}_i denotes the skipped component. Eq. (66) suggests a network structure for the Dual-Frame U-Net. More specifically, unlike the U-Net, the *residual signal* at the low resolution should be upsampled through the unpooling layer. This can be easily implemented using additional by-pass connection for the low-resolution signal as shown in Fig. 2(b). This simple fix allows our network to satisfy the frame condition (36). We suggest the interested readers to consult [47] for further details.

4. Network Design and Training

Let us now design the U-Net and Dual-Frame U-Net neural networks for the elastic source imaging based on the analysis performed in the previous section.

For simplicity, we consider the two-dimensional (2D) case (i.e., $d = 2$) for the recovery of the x -component (i.e., $[\mathbf{F}]_1$) of the unknown source. The y -component (i.e., $[\mathbf{F}]_2$) of the source can be obtained in exactly the same fashion using the same network architectures as discussed in this section.

4.1. Description of the Forward Solver and Time-Reversal Algorithm

For numerical illustrations and generation of the training data, the region of interest Ω is considered as a unit disk centered at origin. Each solution of the elastic wave equation is computed over the box $B = [-\beta/2, \beta/2]^2$ so that $\Omega \subset B$, i.e., $(\mathbf{x}, t) \in [-\beta/2, \beta/2]^2 \times [0, t_{\max}]$. We choose $\beta = 4$ and $t_{\max} = 2$ whereas the temporal and spatial discretization steps are, respectively, chosen to be $h_t = t_{\max}/2^6$ and $h_x = \beta/2^7$. The Lamé parameters are chosen in such a way that the pressure and the shear wave speeds in the medium are, respectively, $c_P = \sqrt{3}m.s^{-1}$ and $c_S = 1m.s^{-1}$.

The Lamé system

$$\begin{cases} \frac{\partial^2 \mathbf{u}}{\partial t^2}(\mathbf{x}, t) - \mathcal{L}_{\lambda, \mu} \mathbf{u}(\mathbf{x}, t) = \frac{\partial \delta_0}{\partial t} \mathbf{F}(\mathbf{x}), & (\mathbf{x}, t) \in \mathbb{R}^2 \times \mathbb{R}, \\ \mathbf{u}(\mathbf{x}, 0) = \mathbf{0} \quad \text{and} \quad \frac{\partial \mathbf{u}}{\partial t}(\mathbf{x}, 0) = \mathbf{0}, \end{cases} \quad (67)$$

is numerically solved over the box B with periodic boundary conditions. A *splitting spectral Fourier* approach [48] is used together with a perfectly matched layer (PML) technique [49] to simulate a free outgoing interface on ∂B . The weighted time-reversal function $\mathcal{I}_{\text{WTR}}(\mathbf{x})$ also requires a Helmholtz decomposition algorithm. Since the support of the function $\mathcal{I}_{\text{WTR}}(\mathbf{x})$ is included in $\Omega \subset B$, a Neumann boundary condition is used on ∂B and a weak Neumann problem is solved in order to derive the Helmholtz decomposition. This decomposition is numerically obtained with a fast algorithm proposed in [50] based on a symmetry principle and a Fourier Helmholtz decomposition algorithm. The interested readers are suggested to consult [44, Sect. 2.2.1] for more details on the numerical algorithm.

4.2. Data Preparation

As a training dataset, $L = 5000$ training pairs $\{(\mathbf{f}_i^{(\ell)}, \mathbf{f}_i^{*(\ell)})\}_{\ell=1}^L$ are generated where $\mathbf{f}_i^{(\ell)}$ is a numerically generated input image and $\mathbf{f}_i^{*(\ell)}$ denotes the synthetic ground-truth phantoms. More specifically, the input images $\{\mathbf{f}_i^{(\ell)}\}_{\ell=1}^L$ are generated numerically by first computing the solution formula for the wave equation for a set of phantom images $\{\mathbf{f}_i^{*(\ell)}\}_{\ell=1}^L$ and then applying the time-reversal algorithm. We centered the pixel values of input images at origin by subtracting the mean intensity of each individual image and dividing it by the maximum value over the entire dataset. The phantoms are generated using the in-built MATLAB *phantom* function such that each phantom had up to ten random overlapping ellipses with their supports compactly contained in Ω . The centers of the ellipses are randomly selected from $[-0.375, 0.375]$. The minor

and major axes are chosen as random numbers from $[-0.525, 0.525]$. The angles between the horizontal semi-axes of the ellipses and the x -axis of the image are also randomly selected from $[-\pi, \pi]$. The intensity values of the ellipses are restricted between $[-10, 10]$ so that the values of the overlapping area are negatively or positively added. Finally, every generated phantom is normalized by subtracting the minimum value and dividing the maximum value sequentially so that its intensity lies in a positive range $[0, 1]$.

4.3. Network architecture

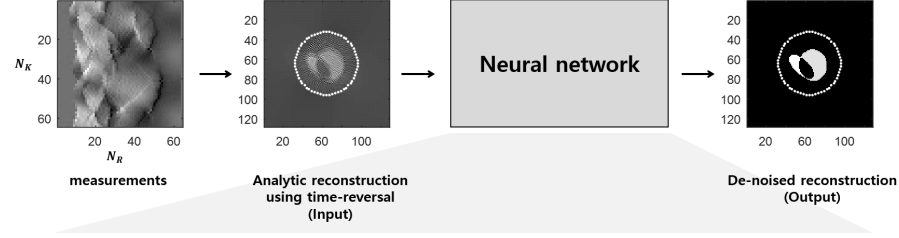
The original and Dual-Frame U-Nets consist of convolution layer, ReLU, and contracting path connection with concatenation (Fig. 3). Specifically, each stage contains four sequential layers composed of convolution with 3×3 kernels and ReLU layers. Finally, the last stage has two sequential layers and the last layer contains only a single convolution layer with 1×1 kernel. The number of channels for each convolution layer is illustrated in Fig. 3. Note that the number of channels is doubled after each max pooling layer. The differences between the original and dual-frame are from additional residual paths illustrated in Fig. 2.

4.4. Network training

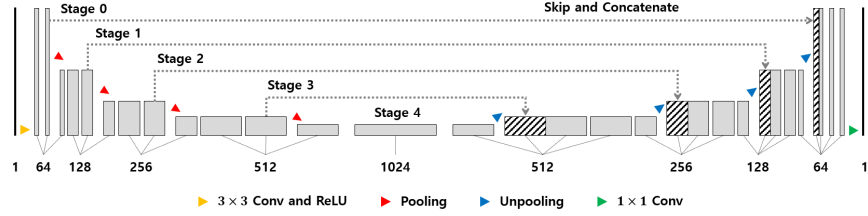
In order to deal with the unbalanced distribution of non-zero values in the label phantom images $\mathbf{f}_i^{*(\ell)}$ and to prevent the proposed network to learning a trivial mapping (rendering all zero values), the non-zero values are weighted by multiplying a constant according to the ratio of the total number of voxel over the non-zero voxels. All the convolutional layers were preceded by appropriate zero-padding to preserve the size of the input. The mean squared error (MSE) is used as a loss function and the network is implemented using Keras library [51]. The weights for all the convolutional layers were initialized using Xavier initialization. The generated data is divided into 4000 training and 1000 validation datasets. For training, the batch size of 64 and Adam optimizer [52] with the default parameters as mentioned in the original paper are used, i.e., the learning rate = 0.0001, $\beta_1 = 0.9$, and $\beta_2 = 0.999$ are adopted. The training runs for up to 200 epochs with early stopping if the validation loss has not improved in the last 20 epochs. We used a GTX 1080 graphic processor and i7-6700 CPU (3.40 GHz). The network took approximately 1300 seconds.

5. Numerical Experiments and Discussion

In this section, we present some numerical realizations of the proposed algorithm for the resolution of the inverse elastic source problem and debate the performance of the proposed deep learning framework. The examples of sparse targets with binary intensities and extended targets with variable intensities are discussed. The sparse targets are modeled by an elongated tubular shape and an ellipse. The extended targets are modeled by the Shepp-Logan phantom. The performance of the proposed framework is compared with the results rendered



(a) *U-net*



(b) *Dual frame U-net*

Figure 3: Schematic illustration

by the weighted time-reversal algorithm with sub-sampled sparse data and total variation (TV) based regularization approach applied on the low-resolution imaging provided by time-reversal algorithm. We compare the reconstructed images under both clean and noisy measurement conditions with the TV-regularization using fast iterative shrinkage thresholding algorithm (FISTA) of Beck and Teboulle [53]. For comparison, we use peak-signal-to-noise ratio (PSNR) and the structural similarity index (SSIM) as metrics. The PSNR and SSIM of the algorithms are calculated as

$$\text{PSNR} := 20 \log_{10} \left(\frac{\tilde{N}\tilde{M}\|\hat{\mathbf{f}}_1\|_{\infty}^2}{\|\hat{\mathbf{f}}_1 - \mathbf{f}_1^*\|_2} \right), \quad (68)$$

$$\text{SSIM} := \frac{\left(2\mu_{\hat{\mathbf{f}}_1}\mu_{\mathbf{f}_1^*} + c_1\right)\left(2\sigma_{\hat{\mathbf{f}}_1\mathbf{f}_1^*} + c_2\right)}{\left(\mu_{\hat{\mathbf{f}}_1}^2 + \mu_{\mathbf{f}_1^*}^2 + c_1\right)\left(\sigma_{\hat{\mathbf{f}}_1}^2 + \sigma_{\mathbf{f}_1^*}^2 + c_2\right)}, \quad (69)$$

where \tilde{M} and \tilde{N} are the number of pixels in the rows and columns, $\hat{\mathbf{f}}_1$ and \mathbf{f}_1^* are the reconstructed image and ground truth, $\mu_{\hat{\mathbf{f}}_1}$ and $\mu_{\mathbf{f}_1^*}$ are the expectations, $\sigma_{\hat{\mathbf{f}}_1}^2$

and $\sigma_{\hat{\mathbf{f}}_1^*}^2$ are the variances, and $\sigma_{\hat{\mathbf{f}}_1^* \mathbf{f}_1^*}^2$ is the covariance of $\hat{\mathbf{f}}_1$ and \mathbf{f}_1^* , respectively. Here, c_1 and c_2 are stabilization parameters and are chosen as $c_1 = (0.01\xi)^2$ and $c_1 = (0.03\xi)^2$ with ξ being the dynamic range of the pixel intensity.

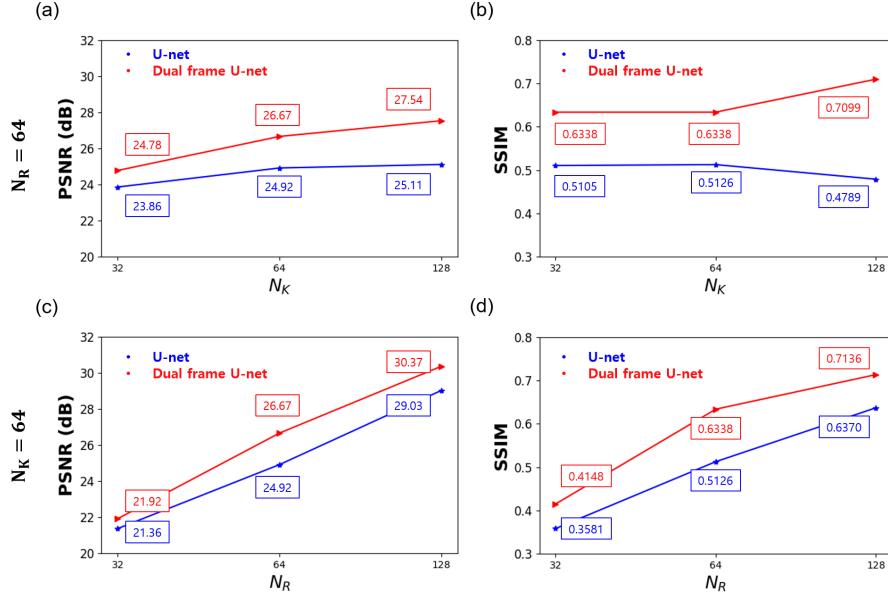


Figure 4: PSNR (left column) and SSIM (right column) results of the standard U-Net (blue) and Dual-Frame U-Net (red).

5.1. Results

Fig. 4 shows the variations of PSNR and SSIM values of the reconstructed test images using the standard and Dual-Frame U-Net. By increasing the number of recorders (N_R) or time steps (N_K), it is observed that the PSNR and SSIM values of the images show a constantly increasing trend except the SSIM value of the image from U-Net with $N_K = 128$ (Fig. 4(b)). On the other hand, the performance of the Dual-Frame U-Net always improved with more measurement data. In addition, the PSNR and SSIM values of the images from the Dual-Frame U-Net are always higher than the ones from the standard U-Net. This suggests that the Dual-Frame U-Net, which satisfies the frame condition, is a robust and predictable reconstruction scheme.

Figs. 5,6 and Figs. 7,8 show the reconstruction results from the test dataset and Shepp-Logan phantom data. In particular, Fig. 5 and Figs. 7 correspond to the noiseless measurements, while Fig. 6 and Figs. 8 are from the noisy measurements. In a noisy condition, a white Gaussian noise with SNR= 5dB is added to the measurement and the images are reconstructed using the time-reversal algorithm. In both conditions, for the total variation algorithm, a

regularization parameter $\gamma = 0.02$ is used without any other constraint and the FISTA algorithm is used. Here, we could not find a significant improvement in the quality of the images by varying the hyperparameter γ . These results are compared with the results by the neural networks which are trained on the images from the clean measurements only. Note that the network has seen neither the images from the noisy measurements nor the Shepp-Logan phantom during the training phase.

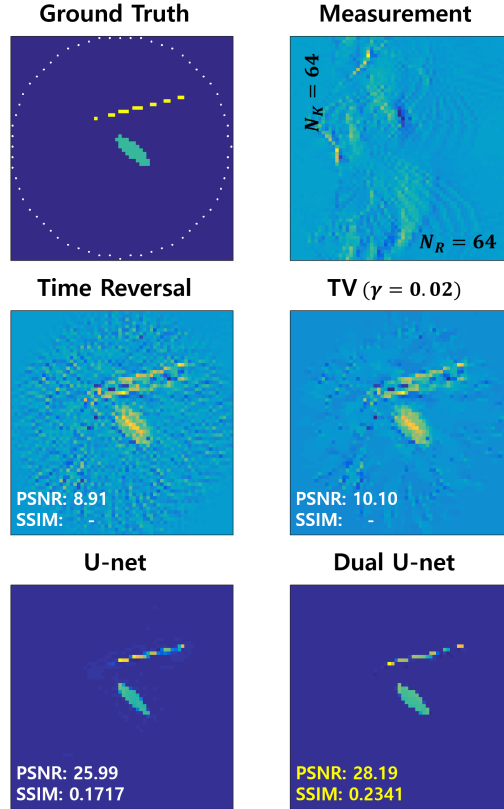


Figure 5: The denoised test dataset images using various algorithms in a clean measurement condition. For a fair comparison, we normalized the pixel values to lie in $[0, 1]$.

5.2. Discussion

The denoising methods using the neural networks showed a superior performance over the total variation algorithm. Among those, the Dual-Frame U-Net showed the best results in both PSNR and SSIM. Though the standard U-Net recovered the overall shape of the inclusions, it failed to find an accurate outfit and lacks the fine details of the inclusions (see Figs. 9–10). For example, the recovered shapes of the ellipses using Dual-Frame U-Net in thin and sparse

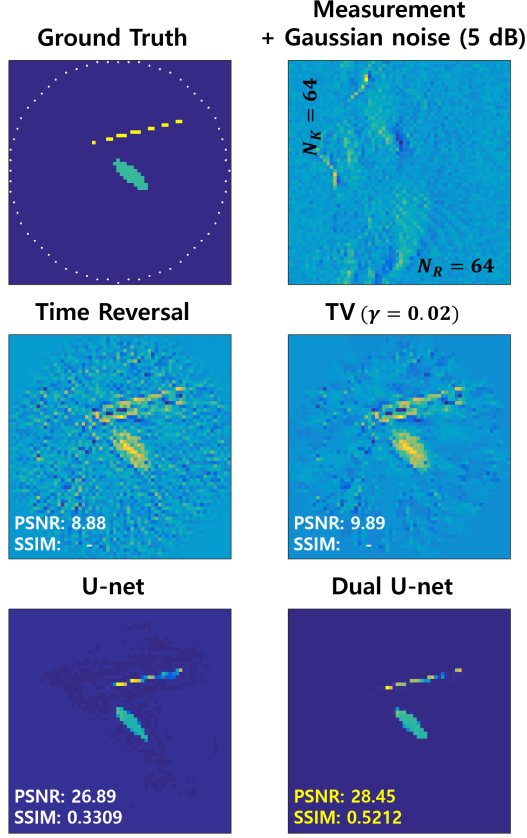


Figure 6: The denoised test dataset images using various algorithms in a noisy measurement condition. For a fair comparison, we normalized the pixel values to lie in $[0, 1]$.

inclusions case have sharper ends than standard U-Net relative to that of the ground truth as highlighted in Fig. 9. In addition, the standard U-Net failed to remove artifacts around the inclusions and bias in the background (Figs. 9–10). On the other hand, the Dual-Frame U-Net recovered the oval shapes of the inclusions and their pixel values more accurately in both sparse and extended targets (pointed out by white arrows in Figs. 9–10). These differences come from the overly emphasized low frequency components in the U-Net configuration that does not meet the frame condition (see, Section 3.3).

6. Conclusion

In this article, we showed that the problem of elastic source imaging with very sparse data, both in space and time, can be successfully dealt with our proposed deep learning framework. While the conventional denoising algorithm

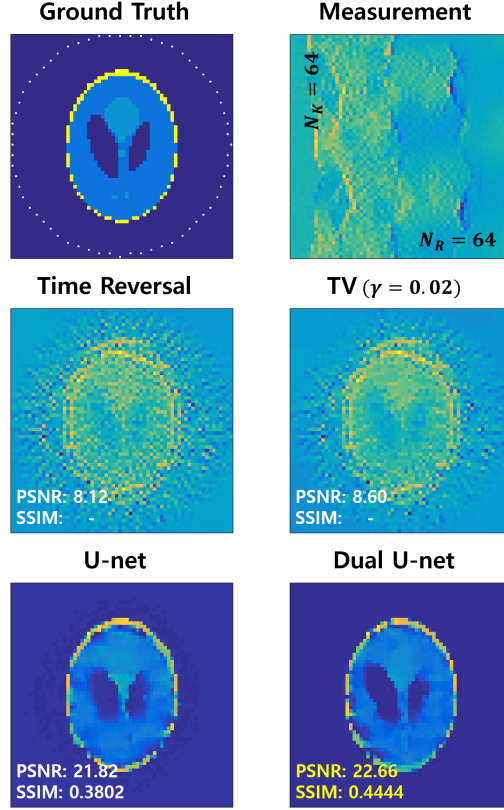


Figure 7: The denoised Shepp-Logan phantom images using various algorithms in a clean measurement condition. For a fair comparison, we normalized the pixel values to lie in $[0, 1]$.

using TV regularization gives an unsatisfying reconstruction quality, deep learning approaches showed more robust reconstruction with better PSNR and SSIM. We showed that the network performance can be further improved by using the Dual-Frame U-Net architecture, which satisfies a frame condition.

Acknowledgment

The authors would like to thank Dr. Elie Bretin for providing the source code for the forward elastic solver and the weighted time-reversal algorithm.

References

- [1] R. P. Porter, A. J. Devaney, Holography and the inverse source problem, *Journal of the Optical Society of America* (1917-1983) 72 (1982) 327.

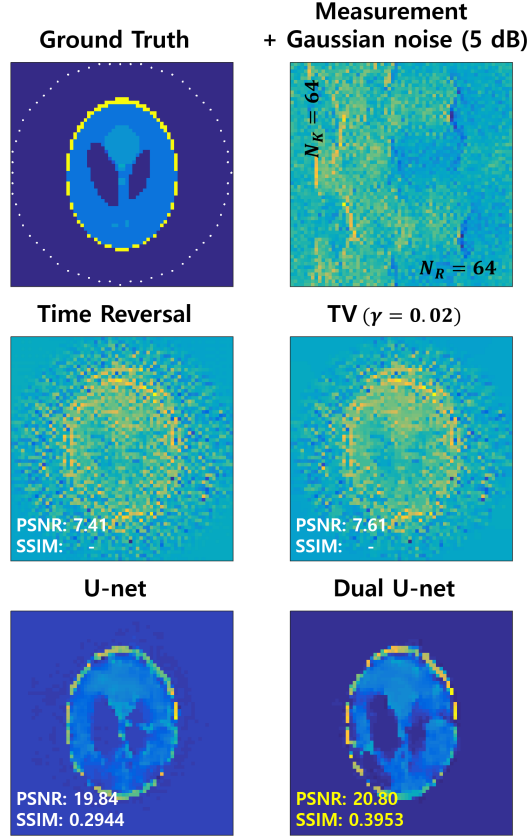


Figure 8: The denoised Shepp-Logan phantom images using various algorithms in a noisy measurement condition. For a fair comparison, we normalized the pixel values to lie in $[0, 1]$.

- [2] C. M. Michel, M. M. Murray, G. Lantz, S. Gonzalez, L. Spinelli, R. G. de Peralta, E?? source imaging, *Clinical Neurophysiology* 115 (10) (2004) 2195 – 2222.
- [3] B. E. Anderson, M. Griffa, T. J. Ulrich, P. A. Johnson, Time reversal reconstruction of finite sized sources in elastic media, *The Journal of the Acoustical Society of America* 130 (4) (2011) EL219–EL225.
- [4] C. Larmat, J.-P. Montagner, M. Fink, Y. Capdeville, A. Tourin, E. Clévédé, Time-reversal imaging of seismic sources and application to the great Sumatra earthquake, *Geophysical Research Letters* 33 (19), l19312.
- [5] S. Kedar, Source distribution of ocean microseisms and implications for time-dependent noise tomography, *Comptes Rendus Geoscience* 343 (2011) 548–557.

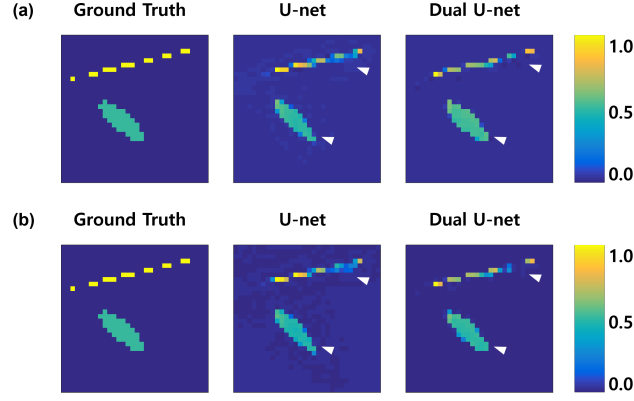


Figure 9: The zoomed-in version of denoised test dataset images in both (a) clean and (b) noisy measurement conditions. For a fair comparison, we normalized the pixel values to lie in $[0, 1]$.

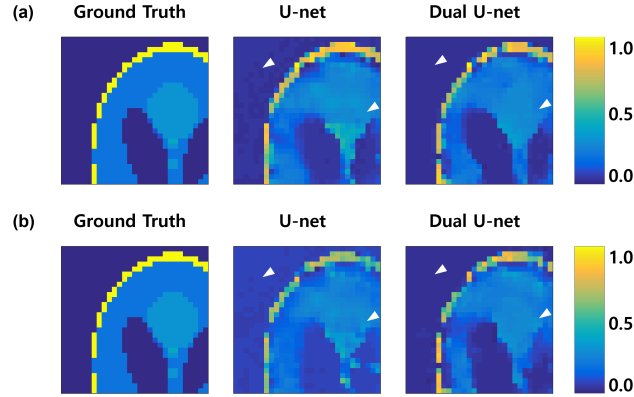


Figure 10: The zoomed-in version of denoised Shepp-Logan phantom images in both (a) clean and (b) noisy measurement conditions. For a fair comparison, we normalized the pixel values to lie in $[0, 1]$.

- [6] A. Archer, K. G. Sabra, Two dimensional spatial coherence of the natural vibrations of the biceps brachii muscle generated during voluntary contractions, in: IEEE Engineering in Medicine & Biology Society (EMBC'10), IEEE, Buenos Aires, Argentina, Piscataway, 2010, pp. 170–173.
- [7] K. G. Sabra, S. Conti, P. Roux, W. A. Kuperman, Passive in vivo elastography from skeletal muscle noise, Applied Physics Letters 90 (19) (2007) 194101.
- [8] J.-L. Gennisson, Transient elastography in anisotropic medium: Applica-

- tion to the measurement of slow and fast shear wave speeds in muscles, *Acoustical Society of America Journal* 114 (2003) 536.
- [9] J. Lim, A. Wahab, G. Park, K. Lee, Y. Park, J. C. Ye, Beyond Born-Rytov limit for super-resolution optical diffraction tomography, *Opt. Express* 25 (24) (2017) 30445–30458.
 - [10] M. Fink, D. Cassereau, A. Derode, C. Prada, P. Roux, M. Tanter, J.-L. Thomas, F. Wu, Time-reversed acoustics, *Reports on Progress in Physics* 63 (12) (2000) 1933.
 - [11] D. Zhang, Y. Guo, J. Li, H. Liu, Locating multiple multipolar acoustic sources using the direct sampling method, *arXiv preprint arXiv:1801.05584*.
 - [12] H. Ammari, E. Bretin, V. Jugnon, A. Wahab, *Photoacoustic Imaging for Attenuating Acoustic Media*, Springer Berlin Heidelberg, Berlin, Heidelberg, 2012, pp. 57–84.
 - [13] A. Lakhal, A. K. Louis, Locating radiating sources for Maxwell’s equations using the approximate inverse, *Inverse Problems* 24 (4) (2008) 045020.
 - [14] R. Albanese, P. B. Monk, The inverse source problem for Maxwell’s equations, *Inverse Problems* 22 (3) (2006) 1023.
 - [15] X. Wang, M. Song, Y. Guo, H. Li, H. Liu, Fourier method for identifying electromagnetic sources with multi-frequency far-field data, *arXiv preprint arXiv:1801.03263*.
 - [16] A. Wahab, A. Rasheed, T. Hayat, R. Nawaz, Electromagnetic time reversal algorithms and source localization in lossy dielectric media, *Communications in Theoretical Physics* 62 (6) (2014) 779.
 - [17] A. Wahab, R. Nawaz, A note on elastic noise source localization, *Journal of Vibration and Control* 22 (7) (2016) 1889–1894.
 - [18] O. Scherzer (Ed.), *Handbook of Mathematical Methods in Imaging*, 1st Edition, Springer, New York, 2011.
 - [19] H. Ammari, J. Garnier, W. Jing, H. Kang, M. Lim, K. Sølna, H. Wang, *Mathematical and Statistical Methods for Multistatic Imaging*, Vol. 2098 of *Lecture Notes in Mathematics*, Springer-Verlag, Chem, 2013.
 - [20] H. Ammari, E. Bretin, J. Garnier, H. Kang, H. Lee, A. Wahab, *Mathematical Methods in Elasticity Imaging*, Princeton University Press, 2015.
 - [21] S. Kremers, A. Fichtner, G. B. Brietzke, H. Igel, C. Larmat, L. Huang, M. Käser, Exploring the potentials and limitations of the time-reversal imaging of finite seismic sources, *Solid Earth* 2 (1) (2011) 95–105.

- [22] M. Griffa, B. E. Anderson, R. A. Guyer, T. J. Ulrich, P. A. Johnson, Investigation of the robustness of time reversal acoustics in solid media through the reconstruction of temporally symmetric sources, *Journal of Physics D: Applied Physics* 41 (8) (2008) 085415.
- [23] E. Kang, J. Min, J. C. Ye, A deep convolutional neural network using directional wavelets for low-dose x-ray CT reconstruction, *Medical Physics* 44 (10).
- [24] H. Chen, Y. Zhang, M. K. Kalra, F. Lin, P. Liao, J. Zhou, G. Wang, Low-dose CT with a residual encoder-decoder convolutional neural network (RED-CNN), *arXiv preprint arXiv:1702.00288*.
- [25] E. Kang, J. C. Ye, Wavelet domain residual network (WavResNet) for low-dose X-ray CT reconstruction, in: 2017 International Meeting on Fully Three-Dimensional Image Reconstruction in Radiology and Nuclear Medicine (arXiv preprint arXiv:1703.01383).
- [26] E. Kang, J. Yoo, J. C. Ye, Wavelet residual network for low-dose CT via deep convolutional framelets, *arXiv preprint arXiv:1707.09938*.
- [27] H. Chen, Y. Zhang, W. Zhang, P. Liao, K. Li, J. Zhou, G. Wang, Low-dose CT via convolutional neural network, *Biomedical optics express* 8 (2) (2017) 679–694.
- [28] J. Adler, O. Öktem, Learned primal-dual reconstruction, *arXiv preprint arXiv:1707.06474*.
- [29] H. Chen, Y. Zhang, W. Zhang, H. Sun, P. Liao, K. He, J. Zhou, G. Wang, Learned experts’ assessment-based reconstruction network (“LEARN”) for sparse-data CT, *arXiv preprint arXiv:1707.09636*.
- [30] T. Würfl, F. C. Ghesu, V. Christlein, A. Maier, Deep learning computed tomography, in: *International Conference on Medical Image Computing and Computer-Assisted Intervention*, Springer, 2016, pp. 432–440.
- [31] Q. Yang, P. Yan, M. K. Kalra, G. Wang, CT image denoising with perceptive deep neural networks, *arXiv preprint arXiv:1702.07019*.
- [32] G. Wang, A perspective on deep imaging, *IEEE Access* 4 (2016) 8914–8924.
- [33] Q. Yang, P. Yan, Y. Zhang, H. Yu, Y. Shi, X. Mou, M. K. Kalra, G. Wang, Low dose CT image denoising using a generative adversarial network with Wasserstein distance and perceptual loss, *arXiv preprint arXiv:1708.00961*.
- [34] J. M. Wolterink, T. Leiner, M. A. Viergever, I. Isgum, Generative adversarial networks for noise reduction in low-dose CT, *IEEE Transactions on Medical Imaging*.
- [35] K. H. Jin, M. T. McCann, E. Froustey, M. Unser, Deep convolutional neural network for inverse problems in imaging, *arXiv preprint arXiv:1611.03679*.

- [36] Y. Han, J. Yoo, J. C. Ye, Deep residual learning for compressed sensing CT reconstruction via persistent homology analysis, arXiv preprint arXiv:1611.06391.
- [37] S. Antholzer, M. Haltmeier, J. Schwab, Deep learning for photoacoustic tomography from sparse data, arXiv preprint arXiv:1704.04587.
- [38] O. Ronneberger, P. Fischer, T. Brox, U-Net: Convolutional networks for biomedical image segmentation, in: International Conference on Medical Image Computing and Computer-Assisted Intervention, Springer, 2015, pp. 234–241.
- [39] J. C. Ye, Y. S. Han, E. Cha, Deep convolutional framelets: A general deep learning framework for inverse problems, SIAM Journal on Imaging Sciences (also available as arXiv:1707.00372), 2018.
- [40] D. L. Donoho, Compressed sensing, IEEE Transactions on Information Theory 52 (4) (2006) 1289–1306.
- [41] J. C. Ye, J. M. Kim, K. H. Jin, K. Lee, Compressive sampling using annihilating filter-based low-rank interpolation, IEEE Transactions on Information Theory 63 (2) (2017) 777–801.
- [42] K. H. Jin, J. C. Ye, Annihilating filter-based low-rank Hankel matrix approach for image inpainting, IEEE Transactions on Image Processing 24 (11) (2015) 3498–3511.
- [43] K. H. Jin, D. Lee, J. C. Ye, A general framework for compressed sensing and parallel MRI using annihilating filter based low-rank Hankel matrix, IEEE Trans. on Computational Imaging 2 (4) (2016) 480–495.
- [44] H. Ammari, E. Bretin, J. Garnier, A. Wahab, Time-reversal algorithms in viscoelastic media, European Journal of Applied Mathematics 24 (4) (2013) 565–600.
- [45] H. Ammari, E. Bretin, J. Garnier, A. Wahab, Time reversal in attenuating acoustic media, Contemporary Mathematics, American Mathematical Society, 2011.
- [46] V. Nair, G. E. Hinton, Rectified linear units improve restricted Boltzmann machines, in: Proceedings of the 27th international conference on machine learning (ICML-10), 2010, pp. 807–814.
- [47] Y. Han, J. C. Ye, Framing U-net via deep convolutional framelets: Application to sparse-view CT, arXiv preprint arXiv:1708.08333.
- [48] C. Canuto, M. Y. Hussaini, A. Quarteroni, A. Thomas Jr, et al., Spectral methods in fluid dynamics, Springer Science & Business Media, 2012.

- [49] F. D. Hastings, J. B. Schneider, S. L. Broschat, Application of the perfectly matched layer (PML) absorbing boundary condition to elastic wave propagation, *The Journal of the Acoustical Society of America* 100 (5) (1996) 3061–3069.
- [50] A. Wiegmann, Fast poisson, fast helmholtz and fast linear elastostatic solvers on rectangular parallelepipeds, Tech. rep., Ernest Orlando Lawrence Berkeley National Laboratory, Berkeley, CA (US) (1999).
- [51] F. Chollet, et al., Keras (2015).
- [52] D. Kingma, J. Ba, Adam: A method for stochastic optimization, arXiv preprint arXiv:1412.6980.
- [53] A. Beck, M. Teboulle, Fast gradient-based algorithms for constrained total variation image denoising and deblurring problems, *IEEE Transactions on Image Processing* 18 (11) (2009) 2419–2434.